

GRAY RADIATION HYDRODYNAMICS WITH THE *FLASH* CODE FOR ASTROPHYSICAL APPLICATIONS

E. CHATZOPOULOS^{1,2}, K. WEIDE²

Draft version January 1, 2018

ABSTRACT

We present the newly–incorporated gray radiation hydrodynamics capabilities of the *FLASH* code based on a radiation flux–limiter aware hydrodynamics numerical implementation designed specifically for applications in astrophysical problems. The newly incorporated numerical methods consist of changes in the unsplit hydrodynamics solver and adjustments in the flux–limited radiation diffusion unit. Our method can treat problems in both the strong and weak radiation–matter coupling limits as well as transitions between the two regimes. Appropriate extensions in the “Helmholtz” equation of state are implemented to treat two–temperature astrophysical plasmas involving the interaction between radiation and matter and the addition of a new opacity unit based on the *OPAL* opacity database, commonly used for astrophysical fluids. A set of radiation–hydrodynamics test problems is presented aiming to showcase the new capabilities of *FLASH* and to provide direct comparison to other codes like *CASTRO*. To illustrate the capacity of *FLASH* to simulate phenomena occurring in stellar explosions, such as shock break–out, radiative precursors and supernova ejecta heating due to the decays of radioactive ⁵⁶Ni and ⁵⁶Co, we also present 1D supernova simulations and compare the computed lightcurves to those of the *SNEC* code. The latest public release of *FLASH* with these enhanced capabilities is available for download and use by the broader astrophysics community.

Subject headings: radiation: dynamics – radiative transfer – methods: numerical

1. INTRODUCTION

The analysis and interpretation of electromagnetic signals is by far the main source of information used to study astrophysical phenomena. In this regard, the importance to understand the interaction between radiation and matter and the physics of radiation transfer is pivotal to gaining comprehensive insights about the underlying physical mechanisms.

Due to the complexity of radiation transport physics combined with the dynamics of strongly ionized plasmas that can, in some cases, possess supersonic motions, most astrophysical problems require numerical simulations for proper examination. A number of codes have been designed that use a multitude of numerical techniques to calculate model light–curves (LCs), spectra, polarization spectra and radiation–driven hydrodynamic flows for direct comparison with observations.

Radiation hydrodynamics (Mihalas & Mihalas 1984; Castor 2007) is necessary to study the propagation and properties of radiative shocks, supernova remnant (SNR) emission, supernova (SN) shock breakout, and radiation–driven mass loss from massive stars near the Eddington limit, to name just a few phenomena. The applicability of the concepts of radiation hydrodynamics in sensitive fields like nuclear weapons simulations and high–energy–density laser experiments has led to the development of codes with such capabilities in government laboratories like the Los Alamos National Laboratory and the Lawrence Berkeley National Laboratory, several of which are inaccessible for use by most academic researchers. Examples of codes used in astrophysical applications that have radiation–hydrodynamics capabilities include *ZEUS* (Stone et al. 1992), *CRASH* (van der Holst et al. 2011), *RAGE* (Gittings et al. 2008) and *CASTRO* (Zhang et al. 2011, 2013), among others.

To model the diffusion of light through expanding matter for the purposes of computing supernova LCs, there are codes that use multi–group time–dependent non–equilibrium radiative transfer (for example, the *STELLA* code of Blinnikov et al. 1998, that incorporates a radiation intensity moments scheme). Frequently, there are simpler numerical approaches used that are based on the flux–limited diffusion approximation (the *SPECTRUM* code of Frey et al. 2013, and the publicly available *SNEC* code of Morozova et al. 2015).

The radiation diffusion approximation is useful in providing us with the general emission properties and model LCs for SNe, but a more rigorous approach requires accurate, time–dependent spectroscopic modeling. Spectroscopic modeling can be computationally expensive, especially in 2D and 3D geometries, because it involves making use of large databases of line opacities in order to calculate emission and absorption line profiles taking into account many factors including material composition, density, temperature and velocity. Currently, the majority of spectral modeling codes are used in a post–processing manner; pure or radiation hydrodynamical “snapshot” profiles are extracted from other codes and then used as inputs to the (usually) Lagrangian grids of radiation transport codes yielding model spectra. A majority of spectral synthesis codes employ Monte Carlo techniques to model radiation transfer and are optimized for both the local (LTE) and non–local thermal equilibrium (nLTE) limits. Examples of some of the most popular codes used include *CMFGEN* (Hillier & Dessart 2012), *SEDONA* (Kasen et al. 2006), *PHOENIX* (Hauschildt & Baron 1999; Hauschildt 1992; Hauschildt & Baron 2004; van Rossum 2012), *SuperNu* (Wollaeger et al. 2013) and the open–source *CLOUDY* (Ferland et al. 1998) and *TARDIS* (Kerzendorf & Sim 2014) codes. Some of these codes have been routinely used to study emission from expanding SN photospheres and have been successfully compared to a lot of observations.

Many of the numerical frameworks summarized above are proprietary or restricted for private use. The advent of open–

chatzopoulos@phys.lsu.edu

¹ Department of Physics & Astronomy, Louisiana State University, Baton Rouge, LA, 70803, USA

² Department of Astronomy & Astrophysics, Flash Center for Computational Science, University of Chicago, Chicago, IL, 60637, USA

source or publicly available computational astrophysics codes like *MESA* (Paxton et al. 2011, 2013, 2015) for stellar evolution, *FLASH* (Fryxell et al. 2000; Dubey et al. 2012) for hydrodynamics, *SNEC* for equilibrium–diffusion radiation transport and *TARDIS* for spectral synthesis has energized the field of computational astrophysics by making these essential modeling tools available for use to everyone in the community, from graduate students to senior researchers, and thus fostering collaboration and transparency. To contribute to this publicly open computational astrophysics endeavor, we introduce our recently implemented gray radiation hydrodynamics scheme of the *FLASH* code optimized for astrophysical applications. Our approach and numerical methods are tested in a variety of contexts and physical domains and benchmarked against the published results of other codes. The latest release of *FLASH* (version 4.5) includes a modified hydrodynamics scheme adjusted for the effects of radiation and improvements in the radiation transfer unit and is available for download. Some documentation is also available within the *FLASH* user’s guide.

The paper is organized as follows. In § 2 we present the set of radiation–hydrodynamics equations in the gray flux–limited diffusion limit that we are numerically solving. In § 3 we discuss in more detail the numerical techniques implemented in the *FLASH* framework to solve that system of equations, namely our radiation flux–limiter aware hydrodynamics (*RadFLAH*) method. A set of test problems illustrating the new capabilities of the code is presented in § 4, and a special application for 1D spherical supernova explosions is discussed in § 5. Finally, in § 6 we discuss our conclusions and the importance of having an open–source tool to study radiation–hydrodynamics in astrophysics.

2. RADIATION HYDRODYNAMICS IN THE FLUX-LIMITED DIFFUSION LIMIT

As a starting point, we take the equations for mixed-frame flux-limited diffusion radiation hydrodynamics developed in Krumholz et al. (2007). Adopting notation for our purposes, we write

$$\frac{\partial \rho}{\partial t} + \nabla \cdot (\rho \mathbf{v}) = 0, \quad (1)$$

$$\frac{\partial (\rho \mathbf{v})}{\partial t} + \nabla \cdot (\rho \mathbf{v} \otimes \mathbf{v}) + \nabla p + \lambda \nabla E_r = 0, \quad (2)$$

$$\begin{aligned} \frac{\partial E_m}{\partial t} + \nabla \cdot [(E_m + p)\mathbf{v}] - \lambda \left(2 \frac{\kappa_P}{\kappa_R} - 1 \right) \mathbf{v} \cdot \nabla E_r \\ = -\kappa_P (4\pi B - cE_r), \end{aligned} \quad (3)$$

$$\begin{aligned} \frac{\partial E_r}{\partial t} + \nabla \cdot [(1 + \lambda')E_r \mathbf{v}] + \lambda \left(2 \frac{\kappa_P}{\kappa_R} - 1 \right) \mathbf{v} \cdot \nabla E_r \\ = \nabla \cdot \left(\frac{c\lambda}{\kappa_R} \nabla E_r \right) + \kappa_P (4\pi B - cE_r). \end{aligned} \quad (4)$$

Here E_m is the matter energy density, defined by the relation $E_m = \rho e_m + \rho \frac{v^2}{2}$ (where e_m is specific internal matter energy), and E_r is the radiation energy density. We make the approximation that the flux limiter λ depends on radiation energy density E_r in the lab frame (rather than a comoving density $E_r^{(0)}$). Thus $\lambda = \lambda(R)$ depends on the quantity $R = \frac{|\nabla E_r|}{\kappa_R E_r}$, and we have further introduced the abbreviation

$\lambda' = \frac{1-f}{2}$, where $f = \lambda + \lambda^2 R^2$ is the Eddington factor. Note that both λ and λ' have similar asymptotic behavior for both the diffusion limit ($\lambda, \lambda' \rightarrow 1/3$ for $R \rightarrow 0$) and the free-streaming limit ($\lambda, \lambda' \rightarrow 0$ for $R \rightarrow \infty$); moreover, as pointed out in Zhang et al. (2011); their difference remains small for all $0 < R < \infty$.

Our implementation uses operator splitting to separate this system of equations into an “enhanced hydro” subsystem and a “radiation transfer” subsystem. The latter describes the effect of the terms written on the right–hand side in Equations 1–4 above, and is equivalent to

$$\rho \frac{\partial e_m}{\partial t} = -\kappa_P (4\pi B - cE_r), \quad (5)$$

$$\frac{\partial E_r}{\partial t} = \nabla \cdot \left(\frac{c\lambda}{\kappa_R} \nabla E_r \right) + \kappa_P (4\pi B - cE_r). \quad (6)$$

The former consists of Equations 1–4 with right hand sides set to 0; we call our approach to solving this system Radiation Flux-Limiter Aware Hydrodynamics (*RadFLAH*). By adding the last two of those modified equations,

$$\frac{\partial E_m}{\partial t} + \nabla \cdot [(E_m + p)\mathbf{v}] - \lambda \left(2 \frac{\kappa_P}{\kappa_R} - 1 \right) \mathbf{v} \cdot \nabla E_r = 0, \quad (7)$$

$$\frac{\partial E_r}{\partial t} + \nabla \cdot [(1 + \lambda')E_r \mathbf{v}] + \lambda \left(2 \frac{\kappa_P}{\kappa_R} - 1 \right) \mathbf{v} \cdot \nabla E_r = 0, \quad (8)$$

we get the following equation:

$$\frac{\partial}{\partial t} (E_m + E_r) + \nabla \cdot [(E_m + p + (1 + \lambda')E_r)\mathbf{v}] = 0. \quad (9)$$

This can also be written

$$\frac{\partial E_{\text{tot}}}{\partial t} + \nabla \cdot [(E_{\text{tot}} + P_{\text{tot}} + p_\Lambda)\mathbf{v}] = 0, \quad (10)$$

with $E_{\text{tot}} = E_m + E_r$ and $P_{\text{tot}} = p + \lambda E_r$ and a small correction term $p_\Lambda = (\lambda' - \lambda)E_r$.

For further reference, we also write an equivalent equation for matter internal specific energy:

$$\frac{\partial (\rho e_m)}{\partial t} + \nabla \cdot (\rho e_m \mathbf{v}) + p \nabla \cdot \mathbf{v} - 2\lambda \frac{\kappa_P}{\kappa_R} \mathbf{v} \cdot \nabla E_r = 0. \quad (11)$$

3. NUMERICAL METHODS

3.1. Modified hydrodynamics.

The goal of the *RadFLAH* code is to solve the (overdetermined) system of five equations (1),(2),(7),(8),(10). This could be done by directly implementing a hyperbolic solver for a system consisting of equations (1), (2), and any two of (7), (8), and (10). We will instead first solve the system of three equations (1),(2),(10) numerically for a time step, thus computing new values of ρ , \mathbf{v} , and total energy E_{tot} , and then use this solution together with (11) and (8) to distribute the total energy change (computed directly from (10)) to the energies E_m and E_r .

FLASH already provides a variety of directionally unsplit methods for solving the system of Euler equations of hydrodynamics (HD), as well as the equations of magnetohydrodynamics (MHD). These are based on the Godunov approach and feature a variety of Riemann solvers, orders of reconstruction, slope limiters, and related features. The HD and MHD

solvers can work with a variety of equation of state (EOS) models by using a formulation derived from [Colella & Glaz \(1985\)](#). In addition to advancing the core variables of HD or MHD, *FLASH* can also advect arbitrary additional variables X (“mass scalars”), equivalent to solving additional equations

$$\frac{\partial(\rho X)}{\partial t} + \nabla \cdot (\rho X \mathbf{v}) = 0. \quad (12)$$

Our approach has been to reuse as much of this existing code as possible. Here we outline this approach; some more implementation details can be found in the appendix.

To discuss our implementation, we write our state in (mostly) conservative form as

$$\mathbf{U} = \begin{pmatrix} \rho \\ \rho \mathbf{v} \\ E_{\text{tot}} \\ \rho e_m \\ E_r \\ X_1 \rho \\ \vdots \\ X_n \rho \end{pmatrix} \quad (13)$$

and our evolution equations as

$$\frac{\partial}{\partial t} \mathbf{U} = f_{\text{hyperbolic}} + f_{\text{fixup}} + f_{\text{Lorentz}} + f_{\text{transp}}. \quad (14)$$

Here

$$f_{\text{hyperbolic}} = \begin{pmatrix} -\nabla \cdot (\rho \mathbf{v}) \\ -\nabla \cdot (\rho \mathbf{v} \mathbf{v}) - \nabla p - \lambda \nabla E_r \\ -\nabla \cdot [(E_{\text{tot}} + P_{\text{tot}} + p_\Lambda) \mathbf{v}] \\ -\nabla \cdot (\rho e_m \mathbf{v}) \\ -\nabla \cdot [(1 + \lambda') E_r \mathbf{v}] \\ -\nabla \cdot (\rho X_1 \mathbf{v}) \\ \vdots \\ -\nabla \cdot (\rho X_n \mathbf{v}) \end{pmatrix}, \quad (15)$$

$$f_{\text{fixup}} = \begin{pmatrix} 0 \\ \mathbf{0} \\ 0 \\ -p \nabla \cdot \mathbf{v} \\ \lambda \mathbf{v} \cdot \nabla E_r \\ 0 \\ \vdots \\ 0 \end{pmatrix}, \quad (16)$$

$$f_{\text{Lorentz}} = \begin{pmatrix} 0 \\ \mathbf{0} \\ 0 \\ 2\lambda \frac{\kappa_P}{\kappa_R} \mathbf{v} \cdot \nabla E_r \\ -2\lambda \frac{\kappa_P}{\kappa_R} \mathbf{v} \cdot \nabla E_r \\ 0 \\ \vdots \\ 0 \end{pmatrix}, \quad (17)$$

and

$$f_{\text{transp}} = \begin{pmatrix} 0 \\ \mathbf{0} \\ \nabla \cdot \left(\frac{c\lambda}{\kappa_R} \nabla E_r \right) \\ -\kappa_P (4\pi B - cE_r) \\ \nabla \cdot \left(\frac{c\lambda}{\kappa_R} \nabla E_r \right) + \kappa_P (4\pi B - cE_r) \\ 0 \\ \vdots \\ 0 \end{pmatrix}. \quad (18)$$

It turns out that the system (1),(2),(10) to be solved already looks like the Euler system *FLASH* can solve, for a fluid consisting of matter and radiation components, with just a few differences:

1. The momentum equation (2) contains a term $\lambda \nabla E_r$ (instead of $\nabla \lambda E_r$; a non-flux-limiter-aware hydro formulation would have the term $\nabla \frac{1}{3} E_r$ here).

We deal with this by advecting additional information from which (for, e.g., the i -direction) the radiation energy $E_{r i \pm 1/2, j, k}$ at cell interfaces can be reconstructed, and then computing $\lambda_{i, j, k} = \frac{E_{r i+1/2, j, k} - E_{r i-1/2, j, k}}{2}$ using λ values computed from the previous solution state.

2. The pressure of the radiation field in the P_{tot} term of the energy equation (10) is reduced to an effective pressure $P_{\text{rad eff}} = \lambda E_r$ by scaling with 3λ . (A non-flux-limiter-aware hydro formulation would have $P_{\text{rad}} = \frac{1}{3} E_r$.)

We deal with this by replacing P_{rad} by $P_{\text{rad eff}}$ in the state that is fed to the hydro solver for reconstruction, flux computation, and updating of conservative variables.

3. The difference between λ and λ' leads to the p_Λ term of energy equation (10).

We can deal with this by advecting a correction and adding it to the fluxes for the energy equation.

3.1.1. Flux computation

Following [Zhang et al. \(2011\)](#) on the gray radiation hydrodynamics implementation in the *CASTRO* code, we note $\lambda \approx \lambda'$ in particular for the [Levermore & Pomraning \(1981\)](#) (LP) flux limiter; we assume in the following that this approximate equality holds true for the flux limiter used. The Godunov method ultimately involves computing fluxes by solving 1D Riemann problems at cell interfaces. Each Riemann problem yields a solution consisting of a “fan” made up of several waves; the number of waves is determined by the number of distinct eigenvalues of a Jacobian matrix of the form

$$\begin{pmatrix} v & \rho & 0 & 0 \\ 0 & v & \frac{1}{\rho} & \frac{\lambda}{\rho} \\ 0 & \gamma p & v & (1 - \gamma) v K \lambda \\ 0 & (\lambda + 1) E_r & 0 & v (K \lambda + 1) \end{pmatrix}$$

derived from the equations, where γ is an effective adiabatic index of the matter that determines the matter-only sound speed, and we use the abbreviation $K = \frac{\kappa_P}{\kappa_R}$.

As shown in Zhang et al. (2011), the set of eigenvalues for a full hyperbolic system, say (1),(2),(7),(8), degenerates to the smaller set of eigenvalues of our system (1),(2),(10) under the approximation $\lambda' = \lambda$, if we further assume $K = 0$. The eigenvalues in this case, $u - c_s, u, u + c_s$ (where u is a velocity component normal to the cell face for which a Riemann problem is solved), depend on the modified sound speed

$$c_s = \sqrt{\gamma \frac{p}{\rho} + (1 + \lambda) \frac{P_{\text{rad eff}}}{\rho}} \quad (19)$$

We note that this is the same sound speed we get with *FLASH* for a fluid composed of matter and (effectively scaled) radiation.

3.2. Flux-limited diffusion solver.

We are using the flux-limited diffusion solver already available in previous versions of *FLASH*. While the default implementation provides for radiation transport in multiple energy groups, we do not yet make use of this multigroup feature for *RadFLASH* applications.

In addition to this default multigroup implementation, *FLASH* also includes an iterative solver for strong radiation-matter coupling as an experimental alternative. This “ExpRelax” implementation of the RadTrans unit is based on the RAGE code paper (Gittings et al. 2008). We use this alternative solver for some of our test problems.

3.3. Extended 2T Helmholtz Equation of State

We have created MatRad3 variants of Eos implementations. These are based on existing *FLASH* code capabilities for 3T Eos models that deal with three independent components (ions, electrons, radiation) of input and output variables, modified to now act on two independent components (matter and radiation). We refer to this approach as 2T(M+R). (The variable slot previously used for electrons is reinterpreted to stand for matter, while the slot for ions is ignored.)

In particular, we have created such a 2T variant of the Helmholtz Eos implementation described in Fryxell et al. (2000) and in the *FLASH* users guide. Since the Helmholtz EOS was already using separate additive components for ions, electrons, and radiation internally, where the electron component essentially depends on temperature and electron density, the changes to the interface have been straightforward.

In addition, some changes were made to make the Helmholtz Eos more robust: when called with a $T < 10^4$ K, the table-based values are extended according to the ideal-gas law.

3.4. Summary of Code Changes

A summary of additions and changes to the *FLASH* code that were implemented as part of this work:

- Modified Hydro:
 - Made “flux-limiter aware” by implementing additional terms described in this paper
 - Optional spatial smoothing of flux limiter variable in Hydro
- 2T (M+R) Helmholtz equation of state.
- Improved Eos robustness (for out-of-range temperatures, etc.).

- OUTSTREAM boundary for free-streaming radiation conditions at the other boundary of a spherical domain.
- Added Opacity implementation that uses OPAL tables.

4. TEST PROBLEMS

The following test problems aim to test the newly implemented *RadFLASH* method in *FLASH* as described in the previous sections. All test problem simulations are done in a 1D spherical grid (except the shock-tube test problem in 1D Cartesian geometry), and the main simulation parameters (domain size, simulation time, resolution, opacities and boundary conditions) are summarized in Table 1. For all tests, the Levermore & Pomraning (1981) (LP) flux-limiter is used. Aside from testing the newly implemented *FLASH* capabilities, we choose our test simulation parameters in a way that we can directly benchmark our results against those of other codes, namely the ones presented by Krumholz et al. (2007) and *CASTRO* (Zhang et al. 2011).

4.1. Propagation of radiation front in the optically-thin regime

In the first test problem, we examine the capacity of our implementation to correctly calculate the properties of a radiation front streaming in the optically-thin limit and its behavior at large distances from the radiating source, tied to the outer radiation boundary conditions. We initialize our grid with a matter temperature and a density profile given by the sigmoid function:

$$X = X_s + \frac{X_{\text{vac}} - X_s}{1 + e^{-\frac{\beta}{r_*}(r-r_*)}}, \quad (20)$$

where $X = \rho, T_m$ and the subscripts “vac” and “s” are used for “vacuum” (the outer, optically-thin region of the domain) and “sphere” (the inner, radiating sphere region) accordingly. The parameter r_* controls the radius where the profile transitions from the sphere to the vacuum and β sets the steepness of this transition. We select $\beta = 30$ and $r_* = 1, 3 \times 10^{11}$ cm for the ρ and T_m , accordingly. We allow the temperature profile to break at a larger radius than the density profile in order to probe the effects of radiation matter coupling in the intermediate region. The radiation temperature (T_r) is initialized to zero throughout the domain in order to force the system to start in an out of equilibrium state. We assume a fully ionized H gas that follows the γ law equation of state (EOS) with $\gamma = 5/3$. Our Rosseland and Plack mean opacity choices (1) imply weak coupling between radiation and matter. In addition, the material is optically-thin outside the radius of the radiating sphere.

Figure 1 shows the final state of our simulation ($t = 10^6$ s). The radiation temperature has fully equilibrated with matter temperature within the optically-thick dense sphere and the radiation energy density (u_r) declines following a r^{-2} law at large distances. This is consistent with the behavior of radiative flux at large distances from a radiating source (the “inverse-square law”: $u_r = L/4\pi r^2$, where L is the intrinsic luminosity of the source and r the distance from the center).

4.2. Radiation-inhibited Bondi accretion

To study the dynamical effects of radiation pressure on matter in the optically-thin limit we simulate the process of radiation-inhibited Bondi accretion (Bondi 1952). A radiating point source of mass M is assumed in the center of the domain, surrounded by a low-density medium. Radiation from

Table 1
Simulation parameters for the *RadFLASH* test problems.

Test problem (§)	ΔR (cm)	t_{sim} (sec)	CFL	Δr_{min} (cm)	κ_{R} (cm^{-1})†	κ_{P} (cm^{-1})†	BC _{hydro} (inner/outer)	BC _{rad} (inner/outer)
§ 4.1†	10^{12}	10^6	0.5	1.953×10^9	4×10^{-6}	4×10^{-10}	reflect extrapolate	reflecting outstream
§ 4.2†	2.5×10^{13}	1.538×10^7	0.8	9.766×10^{10}	0.4	0.0	user user	dirichlet dirichlet
§ 4.3	100	10^{-6}	0.8	0.781	1×10^8	1×10^6	outflow outflow	vacuum vacuum
§ 4.4 – Case 1	10^{14}	10^6	0.6	9.766×10^{10}	2×10^{-10}	2×10^{-16}	reflect outflow	vacuum vacuum
§ 4.4 – Case 2	10^{14}	10^6	0.6	9.766×10^{10}	2×10^{-10}	2×10^{-7}	reflect outflow	vacuum vacuum

Note. — Where ΔR is the size of the computational domain (in 1D spherical coordinates), t_{sim} the total simulation time, CFL the CFL number, Δr_{min} the maximum resolution (or minimum cell size), κ_{R} and κ_{P} the transport (Rosseland) or absorption (Planck) mean opacity accordingly and BC_{hydro}, BC_{rad} the outer boundary condition chosen for hydrodynamics and radiation respectively. † The chosen input opacities for these tests are in units of $\text{cm}^2 \text{g}^{-1}$. For more details on the specifics of the chosen boundary conditions please refer to the *FLASH* user guide.

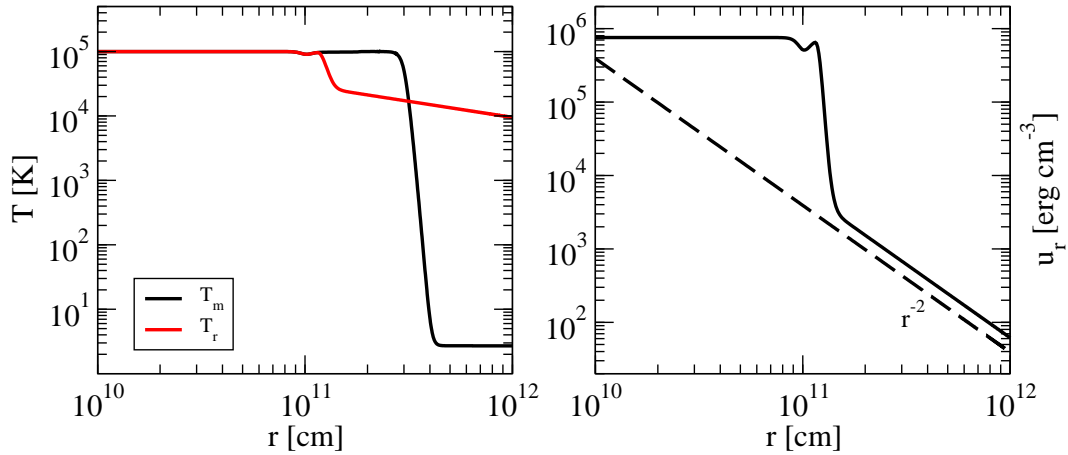


Figure 1. Profiles of matter (T_m ; solid black curve) and radiation (T_r ; solid red curve) temperature (*left panel*) and radiation energy density (u_r ; solid black curve, *right panel*) for the radiating sphere test problem (§ 4.1) at the end of the simulation ($t = 10^6$ s). The dashed black curve in the right panel denotes a $u_r \sim r^{-2}$ decline law.

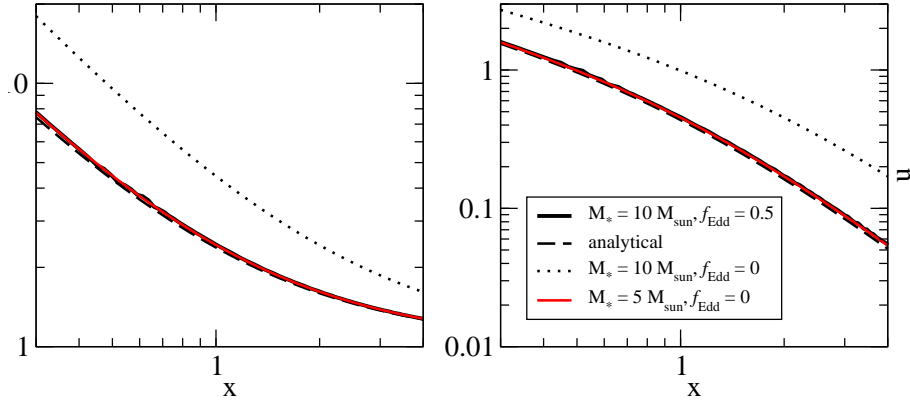


Figure 2. Profiles of scaled density (*left panel*) and scaled radial velocity (*right panel*) for the radiation-inhibited Bondi accretion test problem (§ 4.2) at the end of the simulation ($t = 1.538 \times 10^7$ s or five Bondi times). The solid black and red curves correspond to central source mass of $10 M_\odot$ and $5 M_\odot$ accordingly. The black dashed curve shows the analytic solution and the black dotted curve the case of accretion in the absence of radiation.

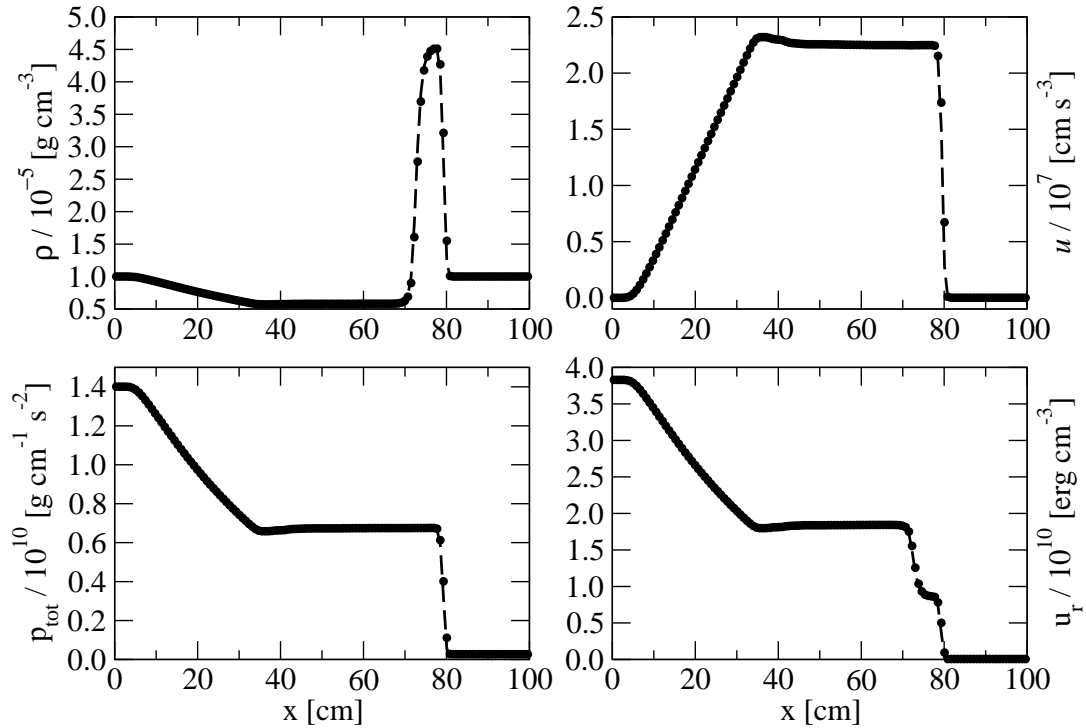


Figure 3. Profiles of density (ρ , *upper left panel*), velocity (u , *upper right panel*), total pressure (p_{tot} , *lower left panel*) and radiation energy density (u_r , *lower right panel*) for the shock-tube problem in the strong coupling limit (§ 4.3) at the end of the simulation ($t = 10^{-6}$ sec). Black dashed curves denote the pure hydrodynamics and filled circles the full radiation hydrodynamics simulation.

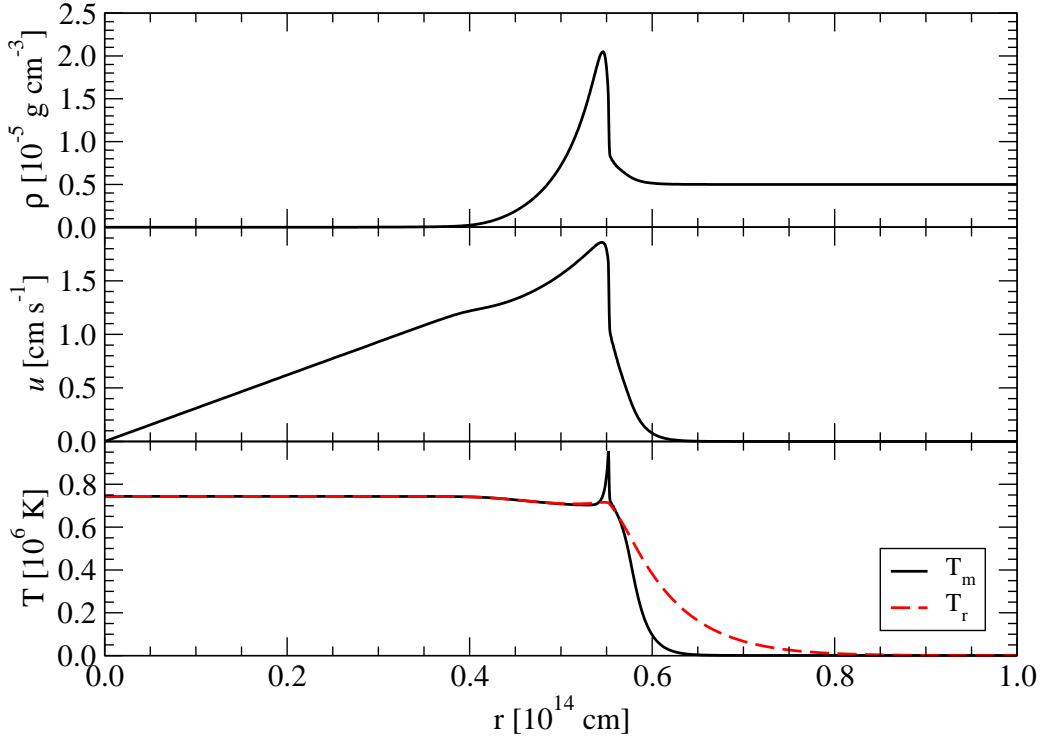


Figure 4. Profiles of density (ρ , upper panel), velocity (u , middle panel) and matter (T_m ; black curves) and radiation (T_r ; red curves) temperature (lower panel) for the radiative shock test problem in the weak coupling limit (§ 4.4) at the end of the simulation ($t = 10^6$ s).

the point source free-streams into the surrounding material exerting force on it, causing the inward spherical accretion onto the gravitating mass to decelerate. The magnitude of the specific (per mass) radiating force on the ambient gas is given by the following expression:

$$f_r = \frac{\kappa_R L}{4\pi r^2 c}, \quad (21)$$

where L is the luminosity of the point source. The ratio of the radiative to the gravitational force is equal to the fraction of the Eddington luminosity with which the central source is radiating:

$$f_{\text{Edd}} = \frac{\kappa_R L}{4\pi G M c}, \quad (22)$$

where G the gravitational constant. Radiation inhibits accretion in a way that is equivalent to the gravitational force by a non-radiating point-source with mass $(1 - f_{\text{Edd}})M$. The time-scale for the accretion system to settle is $\simeq r_B/c_s$ where r_B is the Bondi radius ($r_B = (1 - f_{\text{Edd}})GM/c_s^2$) and c_s the speed of sound in the ambient medium. Assuming an isothermal gas, analytical solutions for the final density and velocity radial profiles can be found by solving the following system of equations (Shu 1992):

$$x^2 \alpha u = \xi \quad (23)$$

$$\frac{u^2}{2} + \ln \alpha - \frac{1}{x} = 0, \quad (24)$$

where $\xi = e^{1.5}/4$ is a constant specific for an isothermal gas, $x = r/r_B$ is the dimensionless radius, $\alpha = \rho/\rho_{\text{vac}}$ the dimensionless density and $u = v/c_s$ the dimensionless velocity.

In this test problem, we use the exact same initial setup as (Krumholz et al. 2007) in order to compare our code with their mixed-frame implementation for radiation hydrodynamics. More specifically, we adopt $\rho_{\text{vac}} = 10^{-18}$ g cm $^{-3}$, $T_{r,\text{vac}} = T_{m,\text{vac}} = 10^6$ K corresponding to $c_s = 1.3 \times 10^7$ cm s $^{-1}$. For the radiating point-source we set $M = 10 M_\odot$ and $L = 1.6 \times 10^5 L_\odot$. Since we are not treating the central source as a sink particle, in contrast with the Krumholz et al. (2007) approach, we employ the Dirichlet option in FLASH for the inner boundary condition for radiation, effectively fixing the radiation and matter temperature in that boundary in a way that it corresponds to the same L . We also enforce radiation-matter coupling by setting $\kappa_P = 0$. With this choice of parameters, $f_{\text{Edd}} = 0.5$, meaning that the effects of radiation-inhibited accretion are equivalent to pure accretion onto a non-radiating point-source with mass $5 M_\odot$.

The simulation is run for five Bondi time-scales and the results are shown in Figure 2. We compare accretion with and without radiation included for the original point source, the

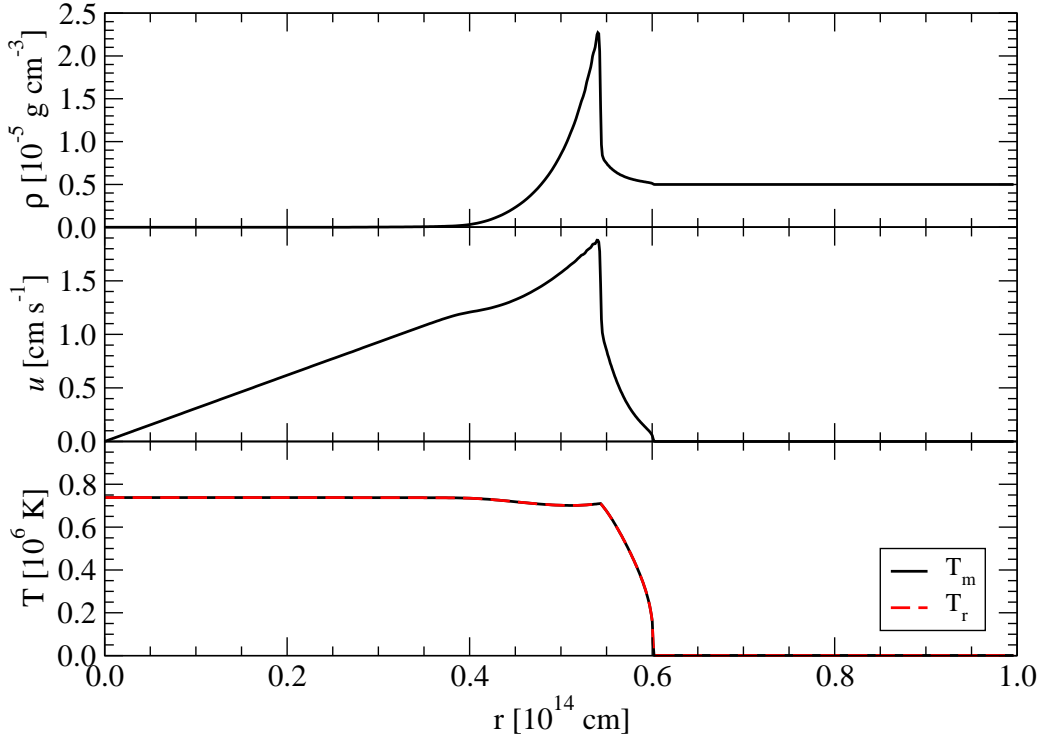


Figure 5. Same as Figure 4 but for the strong coupling limit (§ 4.4).

analytical solution and accretion without radiation included for a point source of half mass ($5 M_{\odot}$). Our results are in very good agreement with the analytical solution and compare well with those of [Krumholz et al. \(2007\)](#) (their Figure 9).

4.3. Shock–Tube problem in the strong coupling limit

To study our implementation in the limit of strong equilibrium and no diffusion we simulate the shock–tube problem. To compare our implementation with results from the *CAS-TRIO* gray radiation hydrodynamics framework, we use the same initial setup as the one presented in [Zhang et al. \(2011\)](#). We divide an 1D Cartesian grid into two distinct regions, separated in the center of the domain at 50 cm that is coincident with a temperature discontinuity. The initial density is uniform throughout the domain and set to $\rho(x) = 10^{-5} \text{ g cm}^{-3}$. The initial velocity is zero everywhere and the initial matter and radiation temperature are set to be equal and initialized in the following way:

$$T_{r,m} = 1.5 \times 10^6 \theta(50 - x) + 3.0 \times 10^5 \theta(x - 50), \quad (25)$$

where $\theta(x - x')$ is the unit step function. We assume the gas to be ideal ($\gamma = 5/3$) with a mean molecular weight $\mu = 1$. Due to the large values for κ_P , κ_R (1), matter and radiation are in strong equilibrium and the domain is optically-thick.

Figure 3 shows the final density, velocity, total (radiation plus gas) pressure and radiation energy density. The full radiation hydrodynamics simulation (filled circles) is compared against a pure hydrodynamics simulation that in the strong–

coupling limit gives almost identical results. This is very well in agreement with the results presented in Figure 8 of ([Zhang et al. 2011](#)).

4.4. Radiative shock in the weak and strong–coupling limit

Given that radiative blast waves are quite common in astrophysical systems and of direct relevance to SNe, this test problem aims to validate the capacity of our implementation to treat shocks both in the weak and the strong radiation–matter coupling limit. More specifically, we evaluate our two implementations for the treatment of radiation transfer: the flux–limited diffusion solver presented in § 3.2 and the iterative solver for strong radiation–matter coupling (the new *ExpRelax* implementation in *FLASH*, § 3.2). To benchmark against *CAS-TRIO* we use the same simulation setups as those presented by [Zhang et al. \(2011\)](#). Specifically, we initialize our domain in 1D spherical coordinates and with a constant–density material, $\rho(r) = 5 \times 10^{-6} \text{ g cm}^{-3}$, at rest ($v(r) = 0 \text{ cm s}^{-1}$) and with a constant radiation and matter temperature set to the same value ($T_{r,m} = 1000 \text{ K}$). We assume ideal gas ($\gamma = 5/3$) with $\mu = 1$. We select our refinement parameters in a way that corresponds to a maximum resolution of $9.766 \times 10^{10} \text{ cm}$, intermediate between the low and high–resolution cases presented in ([Zhang et al. 2011](#)).

In the weak–coupling limit we take the ratio of the emission/absorption to the transport opacity to be $\kappa_P/\kappa_R = 10^{-6}$. In this case, radiation is free to escape in front of the shock forming a radiative precursor and, over time, the radiation and matter temperature depart from equilibrium. In the strong–

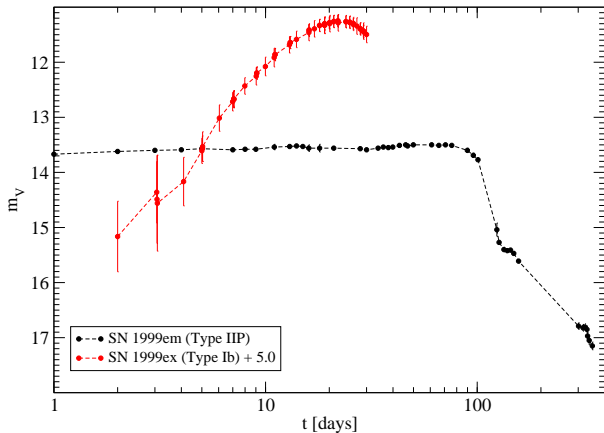


Figure 6. Observed V-magnitude LCs of the Type IIP SN 1999em (Leonard et al. 2002) and the Type Ib SN 1999ex (Stritzinger et al. 2002).

coupling limit we take the opacity ratio to be $\kappa_P/\kappa_R = 1000$. In this case, T_r and T_m remain in equilibrium throughout the simulation and the result is expected to be identical to the corresponding pure 1-T hydrodynamics case. Figures 4 and 5 show the results at the end of the simulations for the weak-coupling and the strong-coupling case accordingly. Again, a great agreement is reproduced between the results of *RadFLAH* and those of Zhang et al. (2011).

5. APPLICATION: 1D SUPERNOVA EXPLOSION

In order to illustrate the capacity of *RadFLAH* to model astrophysical phenomena, we model the LCs of SNe coming from two different progenitor stars: a red supergiant (RSG) star with an extended hydrogen envelope and a more compact blue supergiant star (BSG) models. The RSG model is expected to produce a Type IIP SN LC with a long (~ 100 d) plateau phase of nearly constant bolometric luminosity (L_{bol}) followed by the late-time decline due to the radioactive decays of ^{56}Ni and ^{56}Co . The BSG model on the other hand, due to the lack of an extended hydrogen envelope and the smaller mass, will produce a Type II or Ib/c SN LC with an 1-2 week long re-brightening phase due to heating by the radioactive decays. Examples of both types of SN LCs are shown in Figure 6. Our model LCs will be compared against those of the *SuperNova Explosion Code* (*SNEC*) (Morozova et al. 2015) using the same input RSG and BSG SN profiles.

5.1. Heating due to radioactive decay of ^{56}Ni and SN ejecta opacity

A new Heat physics unit was implemented in *FLASH* to treat the heating of the SN ejecta due to γ -rays produced by the radioactive decays of ^{56}Ni and ^{56}Co . The method used to re-calculate the specific internal energy added in each zone is entirely based on Swartz et al. (1995) and it is the same technique incorporated in *SNEC* and described in the code’s users guide online¹.

This method involves solving the radiation transfer equation in the gray approximation assuming γ -ray opacity, $\kappa_\gamma =$

$0.06Y_e \text{ cm}^2 \text{ g}^{-1}$, where Y_e is the electron fraction. The algorithm loops through all radial zones and calculates the integrated intensity of radiation coming from paths originating from a central spherical region where ^{56}Ni is concentrated (Figure 7). To determine the radius of the ^{56}Ni sphere we set a threshold on the ^{56}Ni mass fraction of 10^{-5} . We then define a radial (N_{radial}) resolution along each path and an angular (N_{angular}) resolution that determines the number of paths originating from the ^{56}Ni sphere that contribute to the heating of each zone. For the models discussed later we use $N_{\text{radial}} = N_{\text{angular}} = 100$. Finally, the internal energy of each zone is updated accordingly by adding that extra heating source term. To preserve a fast running-time, we only add the radioactive decay heating periodically, every one day (86,400 s) throughout the run.

Given our objective to model radiation diffusion through SN ejecta, a new *FLASH* Opacity was developed that takes advantage of the Lawrence Livermore National Laboratory (LANL) *OPAL* opacity database (Iglesias & Rogers 1996). We specifically used opacity tables in two temperature regimes: the low ($\log T < 4.5$; Ferguson et al. 2005) and the high-temperature ($\log T > 4.5$; Grevesse & Sauval 1998) regime based on solar metal abundances. We directly linked the *OPAL* tables from the stellar evolution *MESA* code opacity database in order to take advantage of the consistent and succinct formatting in these files. In order to be provided with a robust comparison against the results of *SNEC*, we had to impose their adopted opacity floor given by:

$$\kappa_{\text{floor}}(r) = \frac{0.24Z_{\text{env}} - 0.01 - 0.23Z(r)}{Z_{\text{env}} - 1}, \quad (26)$$

where Z_{env} is the metallicity of the stellar envelope and $Z(r)$ the metallicity as a function of radius.

5.2. Input SN ejecta profiles

Figure 8 shows the initial structural properties (ρ , T and composition) of the basic RSG and BSG models used taken from the available profiles within the *SNEC* source tree (15MsolRSG and stripped_star therein). In *SNEC* it is emphasized that these models were evolved to the pre-SN stage using the *MESA* code. The RSG model represents a red supergiant star that was $15 M_\odot$ at Zero Age Main Sequence (ZAMS) while the BSG a compact blue star from a $15 M_\odot$ ZAMS model where the convective envelope was stripped during the evolution (Piro & Morozova 2014). Considering mass-loss during the evolution, the final, pre-explosion models had total masses of $12.2 M_\odot$ (RSG) and $4.9 M_\odot$ (BSG).

SNEC provides the user with the option to set a total ^{56}Ni mass as an input and the option to apply one-dimensional parameterized mixing due to the Rayleigh-Taylor and Richtmyer-Meshkov instabilities the SN ejecta using the boxcar smoothing method (Kasen & Woosley 2009). In order to investigate these effects we run three *SNEC* models for each progenitor: one with $M_{\text{Ni}} = 0.05 M_\odot$ using the original SN ejecta profiles, one with $M_{\text{Ni}} = 0.05 M_\odot$ but with boxcar smoothing applied, and one with no ^{56}Ni radioactive decay contributions for a total of six *SNEC* models. For all three RSG’ models and the BSG model with boxcar mixing applied run in *SNEC*, we extract density, temperature and velocity profiles at a time prior to SN shock break-out and when the shock front is a few tenths of a solar mass within the photosphere (taken to be at optical depth of 2/3). Also, since *SNEC* does not use nuclear reaction networks and no

¹ <https://stellarcollapse.org/SNEC>

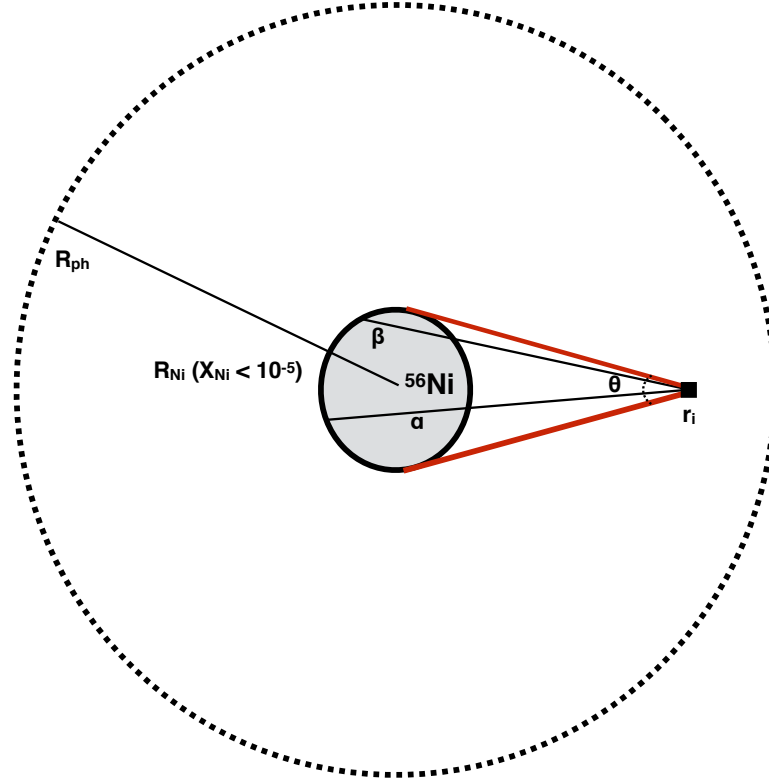


Figure 7. Illustration of the method used to calculate updated specific internal energy in the star due to heating by the ^{56}Ni and ^{56}Co radioactive decays. R_{ph} and R_{Ni} refer to the radii of the photosphere and the ^{56}Ni sphere respectively defined by the location where $X_{\text{Ni}} < 10^{-5}$. The zone in location r_1 in the SN ejecta is heated by the decay of radioactive material spanning an angle θ . We consider an angular resolution $(\theta/N_{\text{angular}})$, where N_{angular} the number of rays extending from the ^{56}Ni sphere to r_1 . For each path (example paths α and β are shown, we also consider a “radial resolution”, N_{radial} , along the path to sum contributions due to heating from all regions of the ^{56}Ni sphere.

nucleosynthesis is performed after the explosion, the initial input model abundance profiles are assumed fixed except for the models for which modifications were applied using box-car averaging. All *SNEC* pre-SN break-out profiles are then mapped into the 1D Adaptive Mesh Refinement (*AMR*) grid of *FLASH* and their evolution is modeled using the *RadFLAH* implementation yielding the computation of gray LCs.

For the *FLASH* simulations we used a simulation box of length 4×10^{16} , large enough to follow the expansion of the SN ejecta for a few hundred days. For this reason we had to include a low-mass circumstellar wind with density scaling as r^{-2} outside the star. The temperature of the wind was kept constant at 100 K and the composition was taken to be the same as that of the outer zone of the stellar model. The presence of wind material around the SN makes the effects of the interaction between the SN ejecta and that wind inevitable, yet minimized in our runs given the low wind density and total mass. To calculate the bolometric gray LCs in *RadFLAH*, a photosphere-locating algorithm was employed that tracks the location of the optical depth $\tau = 2/3$ surface over time and uses the local conditions there to estimate the emergent luminosity.

5.3. SN lightcurves with *RadFLAH*

Figure 9 shows comparisons between the *SNEC* and *FLASH RadFLAH* LCs for the RSG (upper panels) and BSG (lower panels) models. The left panels are a zoom-in to the early

shock break-out and “fireball” expansion phase while the right panels show the total LC evolution, including re-heating of the SN ejecta due to the radioactive decay of ^{56}Ni . The comparison between the shock-breakout LCs indicates that the *FLASH RadFLAH* models exhibit a less luminous yet longer-lasting break-out phase for both the RSG and BSG model, although the total radiated energy is about the same. These differences are attributed to two factors. First and foremost, the two-temperature (2T) treatment where we allow the material and radiation temperature to de-couple in *RadFLAH* while there is just one combined temperature used in *SNEC*. During shock break-out in SNe, 2T effects are strong in the weak coupling limit (see also 4.4). This includes the effect of a radiative precursor leaking ahead of the shock and heating the surrounding medium thus driving the radiation temperature at the photosphere to lower values. Secondly, in contrast with the *SNEC* setup we include a low-density wind around the star that can also influence the properties of shock break-out emission.

The later, re-brightening phases due to the deposition of gamma-rays to the SN ejecta by ^{56}Co decay are in good agreement with the *SNEC* results for both models. The ~ 100 d plateau phase for the RSG models is reproduced at a luminosity of $\sim 3 \times 10^{42}$ erg s^{-1} that is typical for Type IIP SN LCs. Also, the late-time (> 100 d) radioactive decay tail that has a characteristic constant decline rate for ^{56}Co

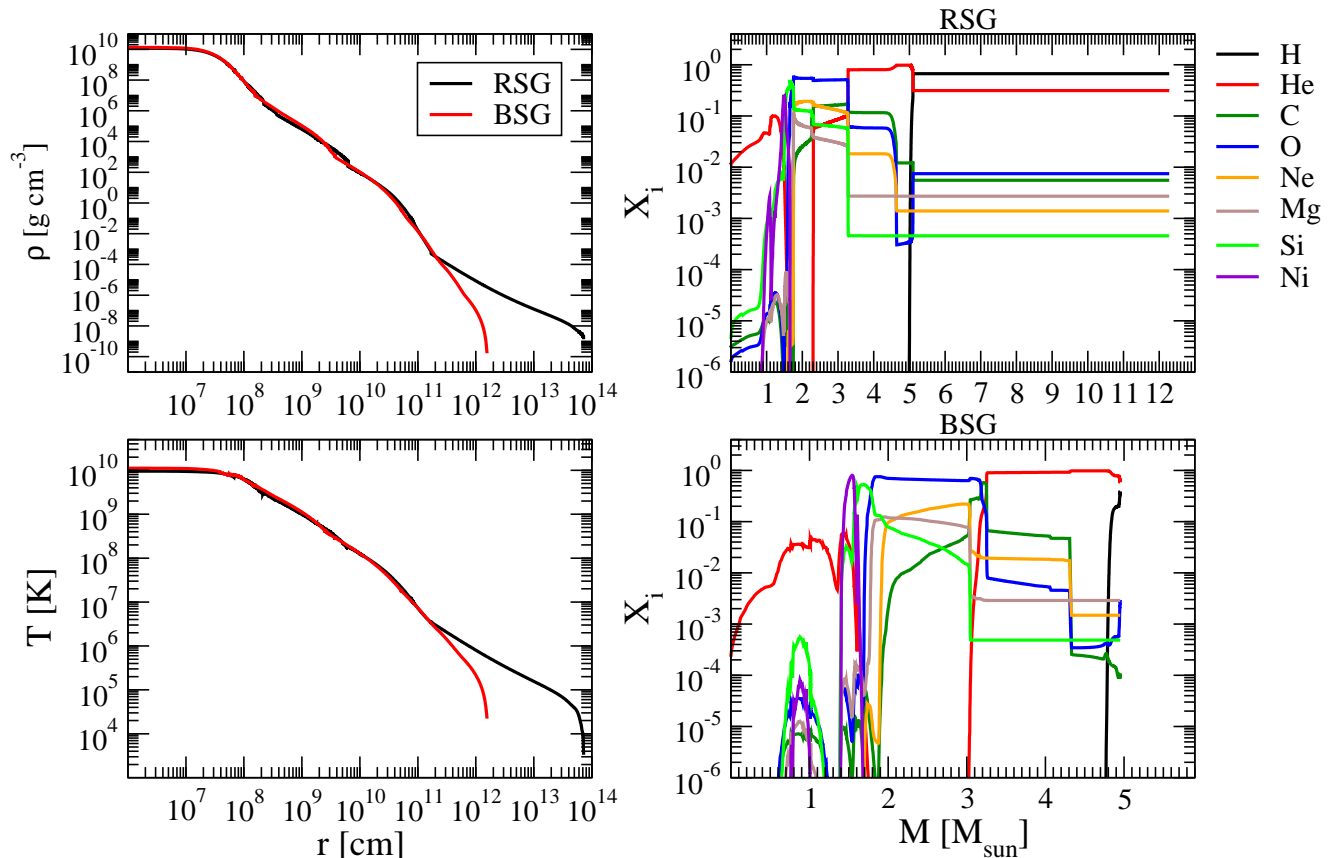


Figure 8. The initial SN profiles used for the calculation of gray LCs with *FLASH RadFLAH*. Density (upper left panel) and temperature (lower left panel) for the RSG (black curves) and BSG (red curves) models. Composition profiles for the RSG (upper right panel) and the BSG (lower right panel) models where no boxcar mixing is applied (5.2).

is reproduced and is consistent with the *SNEC* results. For the RSG model with $M_{\text{Ni}} = 0$ there are considerable differences between the *SNEC* and *FLASH RadFLAH* results at late times after the plateau, with the *FLASH RadFLAH* models exhibiting a much faster decline in luminosity. The *FLASH RadFLAH* result is more in line with the predictions of analytical models for Type IIP LCs like that of Arnett & Fu (1989), given that the effective opacity drops to zero after the end of the hydrogen recombination phase and luminosity should quickly decline during the nebular phases. Similar “tail-less” Type IIP SN LC models in the context of pulsational pair–instability explosions from massive progenitor stars were computed by Woosley (2017) featuring rapid decline rates once the hydrogen recombination front recedes inwards. Another source of this discrepancy is the post–plateau opacities adopted in the *SNEC* code attempting to take into account effects due to dust formation in the SN ejecta at late times and low–temperature conditions (Ferguson & Dotter 2008).

The BSG LC models are also in good agreement between the two codes and are characterized by a faster LC evolution attributable to the smaller initial radius and envelope mass for these progenitors yielding a characteristic Type Ib/c or Type

II LC shape. The same effect of a more smeared–out shock break–out LC is observed here as was the case for the “RSG” model but the later evolution and the ^{56}Ni decay tail are in great agreement between *SNEC* and *FLASH RadFLAH*.

Given the many differences in the treatment of radiation diffusion between the two codes, the initial setup requiring the presence of a circumstellar wind in *FLASH* and discrepancies in the overall numerical implementation, the agreement between the two codes is intriguing and illustrates the capacity of the new *RadFLAH* implementation to provide basic 2T modeling for explosive astrophysical flows including SNe and interaction of SN ejecta with circumstellar matter (CSM).

6. DISCUSSION

The multi–physics, multi–dimensional AMR code *FLASH* has been used for studies of the hydrodynamics of astrophysical systems extensively in the past (Calder 2005; Chatzopoulos et al. 2013; Couch & Ott 2013; Chatzopoulos et al. 2014; Klassen et al. 2014; Couch & Ott 2015; Couch et al. 2015; Chatzopoulos et al. 2016; Klassen et al. 2016). Although a three–temperature (electron, ion and radiation temperature) radiation diffusion scheme was already present in *FLASH*, it was tailored for the treatment of high energy density and laser

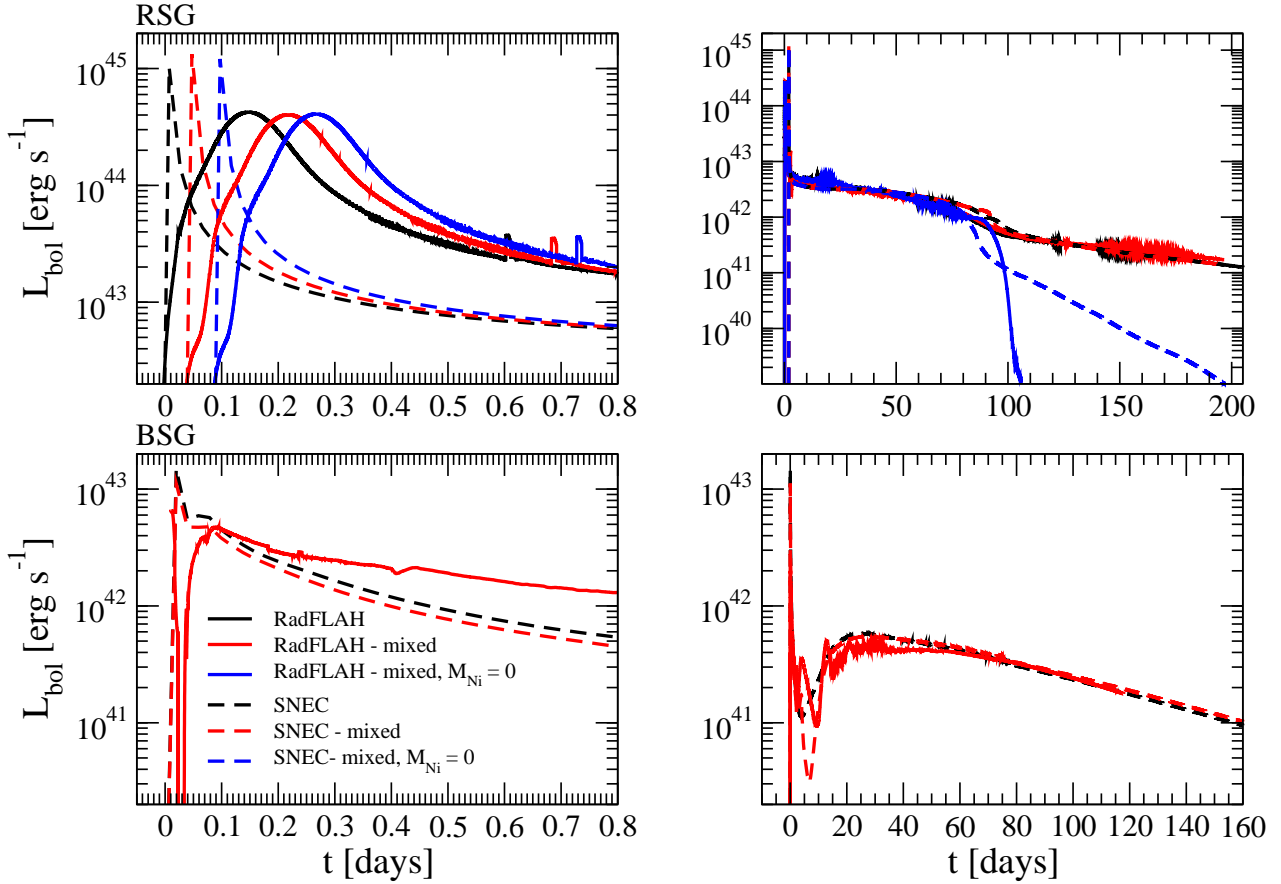


Figure 9. Comparison between *FLASH RadFLAH* (solid curves) and *SNEC* (dashed curves) SN LCs. The upper panels show the results for the “RSG” models and the lower panels those for those “BSG” model. The left panels show a 0.8 day zoom–in the early shock–breakout LCs while the right panels the full LC. The agreement between the two codes is reasonably good given differences in the numerical treatment of radiation diffusion and microphysics.

physics problems and direct application for physical regimes that are appropriate for astrophysical objects was not feasible.

For this reason, we extended the hydrodynamics capabilities of the unsplit hydrodynamics solver available in *FLASH* and implemented the new Radiation Flux–limiter Aware Hydrodynamics (*RadFLAH*) framework able to treat astrophysical problems by evolving the radiation and matter separately in a two–temperature approach and in the gray approximation using the Levermore–Pomraning approximation for the flux limiter.

To be able to utilize our method for astrophysical applications, we implemented an extension of the existing “Helmholtz” equation of state in *FLASH* to lower temperature and density regimes characteristic of stellar photospheres and circumstellar environments. We also introduced a new opacity unit linking the *OPAL* opacity database to obtain transport opacity values as a function of local temperature, density and composition. Finally, we introduced a commonly–used method to treat the deposition of gamma–rays to the SN ejecta due to the ^{56}Co and ^{56}Ni radioactive decay heating as necessary in order to calculate complete SN

LCs to late times after the explosion.

We compared the capabilities of the *FLASH RadFLAH* implementation to those of other codes like *CASTRO* (Zhang et al. 2011) and the Krumholz et al. (2007) code by running standard radiation hydrodynamics and radiation diffusion test problems identical to some of those presented in their methods papers and found very consistent results. Finally, we performed a direct code–to–code comparison with the Supernova Explosion Code (*SNEC* Zhang et al. (2011)) in order to assess our computed SN LCs for two modes: a red supergiant progenitor with an extended hydrogen envelope and a more compact blue supergiant progenitor that experienced strong mass–loss during its evolution, originally performed with the *MESA* stellar evolution code. Given differences in the numerical treatment of hydrodynamics (two–temperature in *RadFLAH* versus one–temperature in *SNEC*) and radiation transfer as well as initial setup (in *FLASH* we had to use a large simulation box and provide data for a low–density circumstellar wind around the progenitor star models), *RadFLAH* LCs were consistent with those computed by *SNEC* for the same initial SN profiles. More specifically, we were able to repro-

duce the characteristics of the main (post break-out) and late-time (radioactive decay “tail”) phase for both models very well. The differences due to our two-temperature treatment and the existence of a low-density wind around the progenitor causing some SN ejecta-circumstellar matter interaction effects, are more prevalent during the early bright shock-break out phase of the LCs. More specifically, we computed shock-break out LCs that reach lower peak luminosities and last longer than the ones found by *SNEC*, yet the total radiated energy throughout this early burst remained consistent.

6.1. Applicability of RadFLAH approach

The *RadFLAH* method is applicable to a variety of astrophysical radiation hydrodynamics problems beyond simple SN LC computations like, for example, studies of SN ejecta-CSM interaction. In a future release we plan to expand the *RadFLAH* capabilities to treat problems in two and three dimensions and for different geometries as well as to incorporate a multi-group treatment for radiation diffusion allowing the user to compute band-specific SN LCs. Given the relatively easy access to the public release of the *FLASH* code and the limited number of public radiation-aware hydrodynamics codes we hope that this new, open framework finds broad appeal in the astrophysics community.

Based on its approximations and assumptions, we expect our method to be particularly useful in regimes that are either close to diffusive or close to free-streaming. The accuracy and stability of the method under conditions of dynamical diffusion (i.e., when $v/c \ll 1$ does not apply) has not been examined and should not be assumed. We expect the method to give good solutions in diffusion-dominated and free streaming regions of a simulation domain; and to sensibly connect such different regions if they exist. We do not expect the solution to be particularly good in regions that cannot be viewed as close to either (statically) diffusive or free-streaming radiation.

Stability of simulations is not always given, in particular due to the time-lagged handling of some quantities in the equations (in particular the flux limiter λ). This is subject to further research.

We would like to thank Daan van Rossum, Mikhail Klassen, Sean M. Couch, Donald Q. Lamb, Carlo Graziani, Petros Tzeferacos, Michael Zingale and the *SNEC* development team for useful discussions and comments. This work was supported in part at the University of Chicago by the U.S. Department of Energy (DOE) under contract B523820 to the NNSA ASC/Alliances Center for Astrophysical Thermonuclear Flashes; the U.S. DOE NNSA ASC through the Argonne Institute for Computing in Science under field work proposal 57789; and by the National Science Foundation under grant AST-0909132. The software used in this work was in part developed by the DOE NNSA-ASC OASCR Flash Center at the

University of Chicago.

REFERENCES

- Arnett, W. D., & Fu, A. 1989, *ApJ*, 340, 396
 Blinnikov, S. I., Eastman, R., Bartunov, O. S., Popolitov, V. A., & Woosley, S. E. 1998, *ApJ*, 496, 454
 Bondi, H. 1952, *MNRAS*, 112, 195
 Calder, A. C. 2005, *Ap&SS*, 298, 25
 Castor, J. I. 2007, *Radiation Hydrodynamics* (Cambridge University Press)
 Chatzopoulos, E., Couch, S. M., Arnett, W. D., & Timmes, F. X. 2016, *ApJ*, 822, 61
 Chatzopoulos, E., Graziani, C., & Couch, S. M. 2014, *ApJ*, 795, 92
 Chatzopoulos, E., Wheeler, J. C., & Couch, S. M. 2013, *ApJ*, 776, 129
 Colella, P., & Glaz, H. M. 1985, *Journal of Computational Physics*, 59, 264
 Couch, S. M., Chatzopoulos, E., Arnett, W. D., & Timmes, F. X. 2015, *ApJL*, 808, L21
 Couch, S. M., & Ott, C. D. 2013, *ApJL*, 778, L7
 —. 2015, *ApJ*, 799, 5
 Dubey, A., Daley, C., ZuHone, J., Ricker, P. M., Weide, K., & Graziani, C. 2012, *ApJS*, 201, 27
 Ferguson, J. W., Alexander, D. R., Allard, F., Barman, T., Bodnarik, J. G., Hauschildt, P. H., Heffner-Wong, A., & Tamanai, A. 2005, *ApJ*, 623, 585
 Ferguson, J. W., & Dotter, A. 2008, in *IAU Symposium*, Vol. 252, *The Art of Modeling Stars in the 21st Century*, ed. L. Deng & K. L. Chan, 1–11
 Ferland, G. J., Korista, K. T., Verner, D. A., Ferguson, J. W., Kingdon, J. B., & Verner, E. M. 1998, *PASP*, 110, 761
 Frey, L. H., Even, W., Whalen, D. J., Fryer, C. L., Hungerford, A. L., Fontes, C. J., & Colgan, J. 2013, *ApJS*, 204, 16
 Fryxell, B., et al. 2000, *ApJS*, 131, 273
 Gittings, M., et al. 2008, *Computational Science and Discovery*, 1, 015005
 Grevesse, N., & Sauval, A. J. 1998, *Space Sci. Rev.*, 85, 161
 Hauschildt, P. H. 1992, *J. Quant. Spec. Radiat. Transf.*, 47, 433
 Hauschildt, P. H., & Baron, E. 1999, *Journal of Computational and Applied Mathematics*, 109, 41
 —. 2004, *A&A*, 417, 317
 Hillier, D. J., & Dessart, L. 2012, *MNRAS*, 424, 252
 Iglesias, C. A., & Rogers, F. J. 1996, *ApJ*, 464, 943
 Kasen, D., Thomas, R. C., & Nugent, P. 2006, *ApJ*, 651, 366
 Kasen, D., & Woosley, S. E. 2009, *ApJ*, 703, 2205
 Kerzendorf, W. E., & Sim, S. A. 2014, *MNRAS*, 440, 387
 Klassen, M., Kuiper, R., Pudritz, R. E., Peters, T., Banerjee, R., & Bunttemeyer, L. 2014, *ApJ*, 797, 4
 Klassen, M., Pudritz, R. E., Kuiper, R., Peters, T., & Banerjee, R. 2016, *ApJ*, 823, 28
 Krumholz, M. R., Klein, R. I., McKee, C. F., & Bolstad, J. 2007, *ApJ*, 667, 626
 Leonard, D. C., et al. 2002, *PASP*, 114, 35
 Levermore, C. D., & Pomraning, G. C. 1981, *ApJ*, 248, 321
 Mihalas, D., & Mihalas, B. W. 1984, *Foundations of radiation hydrodynamics* (Oxford University Press)
 Morozova, V., Piro, A. L., Renzo, M., Ott, C. D., Clausen, D., Couch, S. M., Ellis, J., & Roberts, L. F. 2015, *ApJ*, 814, 63
 Paxton, B., Bildsten, L., Dotter, A., Herwig, F., Lesaffre, P., & Timmes, F. 2011, *ApJS*, 192, 3
 Paxton, B., et al. 2013, *ApJS*, 208, 4
 —. 2015, *ApJS*, 220, 15
 Piro, A. L., & Morozova, V. S. 2014, *ApJL*, 792, L11
 Shu, F. H. 1992, *The physics of astrophysics. Volume II: Gas dynamics*. (University Science Books)
 Stone, J. M., Mihalas, D., & Norman, M. L. 1992, *ApJS*, 80, 819
 Stritzinger, M., et al. 2002, *AJ*, 124, 2100
 Swartz, D. A., Sutherland, P. G., & Harkness, R. P. 1995, *ApJ*, 446, 766
 van der Holst, B., et al. 2011, *ApJS*, 194, 23
 van Rossum, D. R. 2012, *ApJ*, 756, 31
 Wollaeger, R. T., van Rossum, D. R., Graziani, C., Couch, S. M., Jordan, IV, G. C., Lamb, D. Q., & Moses, G. A. 2013, *ApJS*, 209, 36
 Woosley, S. E. 2017, *ApJ*, 836, 244
 Zhang, W., Howell, L., Almgren, A., Burrows, A., & Bell, J. 2011, *ApJS*, 196, 20
 Zhang, W., Howell, L., Almgren, A., Burrows, A., Dolence, J., & Bell, J. 2013, *ApJS*, 204, 7

APPENDIX

We show here in detail how the *RadFLAH* algorithm is implemented in *FLASH* 4.5.

To discuss our implementation in more detail, in a 2T(M+R) formulation, we write our state in (mostly) conservative form as

introduced above,

$$\mathbf{U} = \begin{pmatrix} \rho \\ \rho \mathbf{v} \\ E_{\text{tot}} \\ \rho e_{\text{m}} \\ E_{\text{r}} \\ X_1 \rho \\ \vdots \\ X_n \rho \end{pmatrix} \quad (27)$$

and our evolution equations as

$$\frac{\partial}{\partial t} \mathbf{U} = f_{\text{hyperbolic}} + f_{\text{fixup1}} + f_{\text{fixup2}} + f_{\text{Lorentz}} + f_{\text{transp}}. \quad (28)$$

To allow for different choices for the implementation of some terms, and allow for parametric control of these for the purpose of experimentation, we introduce numerical parameters $\alpha_{\text{m}}, \alpha_{\text{r}}, \beta_{\text{m}}, \beta_{\text{r}} \in [0, 1]$. These control, separately for both matter and radiation components of energy, whether (and, if we allow them to have non-integer values, to what degree):

- pressure terms are included in the conservative fluxes ($\alpha_{\text{m,r}}$),
- work terms are implemented explicitly ($\beta_{\text{m,r}}$),

and we require

$$\alpha_c + \beta_c \leq 1 \quad \text{for } c \in \{\text{m}, \text{r}\}.$$

In case we want the dominant changes of $E_{\text{m}}, E_{\text{r}}$ that go beyond simple advection to be completely represented by explicit terms in $f_{\text{hyperbolic}}$ and f_{fixup1} , we have to set $\alpha_c + \beta_c = 1$. If, on the other hand, we want those changes to be handled by the f_{fixup2} term, we set $\alpha_c = \beta_c = 0$.

Then

$$f_{\text{hyperbolic}} = \begin{pmatrix} -\nabla \cdot (\rho \mathbf{v}) \\ -\nabla \cdot (\rho \mathbf{v} \mathbf{v}) - \nabla p - \lambda \nabla E_{\text{r}} \\ -\nabla \cdot [(E_{\text{tot}} + P_{\text{tot}} + p_{\Lambda}) \mathbf{v}] \\ -\nabla \cdot (\rho e_{\text{m}} \mathbf{v} + \alpha_{\text{m}} p \mathbf{v}) \\ -\nabla \cdot [(1 + \alpha_{\text{r}} \lambda) E_{\text{r}} \mathbf{v} + p_{\Lambda} \mathbf{v}] \\ -\nabla \cdot (\rho X_1 \mathbf{v}) \\ \vdots \\ -\nabla \cdot (\rho X_n \mathbf{v}) \end{pmatrix}, \quad (29)$$

$$f_{\text{fixup1}} = \begin{pmatrix} 0 \\ \mathbf{0} \\ 0 \\ -\beta_{\text{m}} p \nabla \cdot \mathbf{v} + \alpha_{\text{m}} \mathbf{v} \cdot \nabla p \\ -\beta_{\text{r}} \lambda E_{\text{r}} \nabla \cdot \mathbf{v} - (1 - \alpha_{\text{r}}) (E_{\text{r}} \mathbf{v} \cdot \nabla \lambda) + \alpha_{\text{r}} \lambda \mathbf{v} \cdot \nabla E_{\text{r}} \\ 0 \\ \vdots \\ 0 \end{pmatrix}, \quad (30)$$

$$f_{\text{fixup2}} = \begin{pmatrix} 0 \\ \mathbf{0} \\ 0 \\ w_{\text{m}} \\ w_{\text{r}} \\ 0 \\ \vdots \\ 0 \end{pmatrix}, \quad (31)$$

Here we have introduced “work-like” quantities w_{m} and w_{r} that represent any changes in the thermal and radiation energies that are not already included in the explicit terms of $f_{\text{hyperbolic}} + f_{\text{fixup1}}$. In numerical application, we first apply the updates $f_{\text{hyperbolic}} + f_{\text{fixup1}}$ terms to a discretized version of \mathbf{U}^n at a time t_n to compute an intermediate state:

$$\tilde{\mathbf{U}}^{n+1} = \mathbf{U}^n + (f_{\text{hyperbolic}} + f_{\text{fixup1}}) \Delta t.$$

This is done by first using a (slightly modified) traditional Godunov method for a conservative update as per $f_{\text{hyperbolic}}$, and then applying additional terms. An important modification is the $-\lambda \nabla E_{\text{r}}$ term in the momentum equation. We currently use

precomputed λ^n values based on the previous time step in the implementation of TRUE?, represented on the same discrete grid used for cell-centered conservative variables. We have implemented numerical spatial smoothing of this flux-limiter variable to counteract instabilities that we found in some simulations.

For the components of U^n we have $E_{\text{tot}} = \rho e_{\text{m}} + E_{\text{r}} + \rho \frac{v^2}{2}$, this will in general not be true for the components of \tilde{U}^{n+1} , and we compute the energy mismatch

$$\Delta E_{\text{tot}} = \widetilde{E}_{\text{tot}} - \left(\tilde{\rho} \tilde{e}_{\text{m}} + \tilde{E}_{\text{r}} + \tilde{\rho} \frac{\tilde{v}^2}{2} \right),$$

where tilde indicates components of \tilde{U}^{n+1} .

Next we reestablish consistency between the energy components by applying the $f_{\text{fixup}2}$ term. Note that we trust the value of $\widetilde{E}_{\text{tot}}$ (as well as $\tilde{\rho}$ and \tilde{v}^2), which come from the conservative update of the hyperbolic system, more than the updated values of \tilde{e}_{m} and \tilde{E}_{r} , so we adjust the latter by partitioning the energy mismatch among them, such that $\Delta E_{\text{tot}} = (w_{\text{m}} + w_{\text{r}}) \Delta t$. We have implemented various strategies for effecting this partitioning. We briefly describe here ‘‘RAGE-like energy partitioning’’ (RLEP), which is based on the same approach that has been implemented in the FLASH code (Release 4 and later) for partitioning of energies between electron and ion components, which in turn is described in [Gittings et al. \(2008\)](#).

Let $q_c = w_c \Delta t$ for $c \in \{\text{m}, \text{r}\}$. Let p^+ , $P_{\text{rad eff}}^+ = \lambda \tilde{E}_{\text{r}}$, and $P_{\text{tot}}^+ = p^+ + P_{\text{rad eff}}^+$ be predicted values of matter, effective radiation, and total pressures, respectively, at time t_{n+1} that can be computed by EOS calls on the \tilde{U}^{n+1} state. Then define

$$q_{\text{m}} = \frac{p^+}{P_{\text{tot}}^+} \Delta E_{\text{tot}}, \quad q_{\text{r}} = \frac{P_{\text{rad eff}}^+}{P_{\text{tot}}^+} \Delta E_{\text{tot}}, \quad (32)$$

i.e., simply partition the energy mismatch in proportion to the pressure ratios. We also use additional fallbacks and heuristics, *e.g.*, to recover from unphysical nonpositive energy values.

The remaining two terms f_{Lorentz} and f_{transp} have already been presented in the main text in (17) and (18).